Simulating electron spin resonance spectra of nitroxide spin labels from molecular dynamics and stochastic trajectories

Deniz Sezer,[1,2] Jack H. Freed,[3] and Benoît Roux[2,a]

[1]*Department of Physics, Cornell University, Ithaca, New York 14853, USA*
[2]*Department of Biochemistry and Molecular Biology, The University of Chicago, Chicago, Illinois 60637, USA*
[3]*Department of Chemistry and Chemical Biology, Cornell University, Ithaca, New York 14853, USA*

Simulating electron spin resonance spectra of nitroxide spin labels from motional models is necessary for the quantitative analysis of experimental spectra. We present a framework for modeling the spin label dynamics by using trajectories such as those from molecular dynamics (MD) simulations combined with stochastic treatment of the global protein tumbling. This is achieved in the time domain after two efficient numerical integrators are developed: One for the quantal dynamics of the spins and the other for the classical rotational diffusion. For the quantal dynamics, we propagate the relevant part of the spin density matrix in Hilbert space. For the diffusional tumbling, we work with quaternions, which enables the treatment of anisotropic diffusion in a potential expanded as a sum of spherical harmonics. Time-averaging arguments are invoked to bridge the gap between the smaller time step of the MD trajectories and the larger time steps appropriate for the rotational diffusion and/or quantal spin dynamics. © *2008 American Institute of Physics*. [DOI: 10.1063/1.2908075]

I. INTRODUCTION

Nitroxide spin labels are extensively used in electron spin resonance (ESR) studies of proteins,[1,2] nucleic acids,[3] and lipid bilayers.[2] The ability to simulate ESR spectra from models of the spin label dynamics is indispensable for the quantitative analysis and interpretation of experimental spectra. Conceptually, the problem can be divided into two complementary parts: Classical and quantum. The dynamics of the coupled electronic-nuclear spin system necessitates a quantum mechanical treatment, whereas the rotational dynamics of the spin label is best treated classically. The classical dynamics may be entirely deterministic, stochastic, or incorporate elements of both. The choice of the model for the classical motion determines the time dependence of the spin Hamiltonian. The latter is used to calculate the relaxation of the transverse magnetization, and henceforth, ESR spectra. As usual when dealing with dynamic stochastic processes, it is possible to work either directly with the probability density or with explicit realizations of the process in the time domain (trajectories). In the former case, the coupled classical-quantum evolution is described by the stochastic Liouville equation (SLE) due to Kubo.[4–6] This approach constitutes the basis of the sophisticated theory and spectral simulation/fitting software developed by Freed and co-workers over the last four decades.[7–13] In this paper, we pursue the second alternative and work with dynamic trajectories.

While the idea of using trajectories to simulate ESR spectra is not new,[14–16] it is becoming increasingly attractive for two main reasons. For instance, it is feasible to generate trajectories for more complicated stochastic models than can readily be handled with the SLE formalism. This has been suggested by Westlund and co-workers,[17,18] although they employ models still tractable with the SLE.[10,11,13] Furthermore, it is possible to directly simulate spectra from deterministic molecular dynamics (MD) trajectories,[19–23] without invoking any stochastic model. The prospect of using atomically detailed MD trajectories to simulate ESR spectra is even more attractive with the recent development of high-field ESR.[24] Increased sensitivity to dynamics on the sub-nanosecond time scale at high fields holds the promise of establishing a tighter connection between MD simulations and experimental spectra, hopefully resulting in the detailed interpretation of the latter and more stringent validation of the former. The current paper is a part of our more extensive effort to use MD trajectories in the simulation of multifrequency ESR spectra.[25]

A major challenge to this effort is that many, long trajectories, far beyond what can be routinely achieved with straightforward MD, are necessary for the convergence of the spectra.[16,21,22,26] As an alternative, MD trajectories can be used to estimate the parameters of a preselected stochastic dynamic model.[20,23,27] ESR spectra are then calculated by either solving the SLE,[27] or generating trajectories,[20,23] for the model. In principle, once the stochastic model and its parameters are established, either the SLE approach or the trajectory-based approach are applicable. In practice, spectra from more sophisticated rotational dynamics models such as microscopic order macroscopic disorder (MOMD) and slowly releasing local structure (SRLS), developed within the SLE formalism,[9–11,13] have not been simulated by using the trajectory-based approach. Previous works in which rotational diffusion trajectories were employed to simulate

a)Electronic mail: roux@uchicago.edu.

ESR spectra were restricted to free isotropic diffusion[15,16] or isotropic diffusion in a cone.[28] The lack of a rigorous formalism to simulate trajectories for anisotropic diffusion in a potential has prevented the trajectory-based approach to be exploited to its fullest.

Here, we address two separate questions pertaining to the simulation of ESR spectra from trajectories. First, what is the most efficient and rigorous way of propagating the quantal spin dynamics and calculating the transverse magnetization, given as many and as long trajectories as necessary? Several quantum integrators achieving this have already been proposed in the literature.[20,26,29] They range from simplified treatment considering only the eigenvalues of the instantaneous Hamiltonian[20] (disregarding the eigenvectors), to the rigorous propagation of the state vector in Hilbert space[26] or the density matrix in Liouville space.[29] We show that, once the high-field approximation is introduced, the most efficient choice is to propagate the density matrix in Hilbert space. Second, how can MD trajectories, necessarily missing information about the global macromolecular dynamics, be utilized in a meaningful way to simulate experimentally relevant ESR spectra? We propose to use the MD trajectories in combination with trajectories from stochastic models, which can account for the dynamical events that are poorly sampled in the MD simulations, such as the tumbling of the spin labeled macromolecule. To this end, an efficient numerical integrator, which enables the generation of trajectories for sophisticated, anisotropic rotational diffusion models such as MOMD and SRLS, is developed. An important issue in establishing a practical algorithm is to bridge the gap between the small time step at which the snapshots along the MD trajectories are available and the longer time steps appropriate for the numerical propagation of the stochastic or quantal dynamics.

The paper is organized as follows: Quantal spin dynamics and classical anisotropic Brownian diffusion in a potential are the subject of Sec. II. The former is reviewed in Sec. II A, in which we illustrate how to numerically propagate the relevant part of the density matrix in Hilbert space. The latter is developed in Sec. II B, in which an accurate and efficient numerical integrator for this general rotational diffusion model is presented. Last, spectra for free and restricted rotational diffusion models simulated by using the developed time-domain integrators and the SLE are compared. Section III contains a proposed strategy for combining MD and stochastic trajectories. Time-averaging arguments are invoked to bridge the gap between the various integration time steps. Multifrequency spectra simulated by using a combination of rotational diffusion/MD trajectories are presented. A concluding discussion is given in Sec. IV. The appendices provide further detail about some expressions used in the numerical work.

II. NUMERICAL INTEGRATORS

A. Integrating the quantal spin dynamics

The formal equivalence between continuous-wave and free induction decay (FID) spectra[30] is exploited to simulate

the latter instead of the former. The efficient numerical simulation of FID ESR spectra is addressed after reviewing the relevant theoretical background.

1. The spin Hamiltonian and the interaction picture

A nitroxide has an unpaired electron with spin $\hat{\boldsymbol{S}}$ $(S = \frac{1}{2})$ and a ^{14}N nucleus with nuclear spin $\hat{\boldsymbol{I}}$ $(I = 1)$. (Throughout, bold letters are used to denote vectors in physical space; Hilbert space operators are indicated with a caret.) The spin Hamiltonian of a nitroxide, in units of angular frequency, is

$$\hat{H}(t) = \gamma_e (\boldsymbol{B} \cdot \mathsf{G}(t) \cdot \hat{\boldsymbol{S}} + \hat{\boldsymbol{I}} \cdot \mathsf{A}(t) \cdot \hat{\boldsymbol{S}}), \tag{1}$$

where γ_e is the electronic gyromagnetic ratio, A is the hyperfine tensor (expressed in units of magnetic field) and

$$\mathsf{G}(t) \equiv \mathsf{g}(t)/g_c \tag{2}$$

is the electronic g tensor $\mathsf{g}(t)$ divided by the free electron g factor g_e. The coupling tensors G and A are typically diagonal in the same coordinate frame N, attached to the nitroxide. Their explicit time dependence in Eq. (1) is due to the dynamics of this frame with respect to the stationary laboratory frame L, in which the external magnetic field $\boldsymbol{B} = (0, 0, B_0)$ is applied. Since the electronic spin is quantized in the laboratory frame, all the vector and tensor components in Eq. (1) are defined with respect to L. The nuclear Zeeman and the quadrupolar interactions are typically neglected, but they can be included in the methodology described below, when needed. Coupling to other spins in the system is typically ignored at this stage.

We denote the quantal state of the electronic and nuclear spins localized on a single spin label by $|\psi(t)\rangle$. The dynamics of this state vector are governed by the spin Hamiltonian through the Schrödinger equation. Let us write the Hamiltonian from Eq. (1) in the form

$$\hat{H}(t) = \hat{H} + \hat{V}(t), \tag{3}$$

where the first part

$$\hat{H} \equiv \gamma_e G_0 B_0 \hat{S}_z = \omega_0 \hat{S}_z, \tag{4}$$

with

$$G_0 \equiv \tfrac{1}{3} \mathrm{Tr}\{\mathsf{G}\}, \tag{5}$$

isolates a large but constant portion of $\hat{H}(t)$. The remaining time-dependent part is contained in $\hat{V}(t)$. In the absence of $\hat{V}(t)$, the state vector oscillates at the Larmor precession frequency ω_0. In its presence, the instantaneous frequency of precession varies around ω_0 by a time-dependent modulation, which is typically much smaller than ω_0.

Explicit treatment of the Larmor precession is inconvenient when the quantum dynamics are numerically integrated, since resolving the fast oscillations requires the use of a small integration time step. This difficulty is readily dealt with by transforming to a coordinate frame rotating at the Larmor frequency (i.e., the interaction picture). In the interaction picture, where

$$|\psi'(t)\rangle \equiv e^{i\hat{H}t}|\psi(t)\rangle, \quad \hat{V}'(t) \equiv e^{i\hat{H}t}\hat{V}(t)e^{-i\hat{H}t}, \qquad (6)$$

the Schrödinger equation is

$$|\dot{\psi}'(t)\rangle = -i\hat{V}'(t)|\psi'(t)\rangle. \qquad (7)$$

(The dot indicates time derivative.) By using the relations

$$\hat{S}'_z = \hat{S}_z, \quad \hat{S}'_+ = \hat{S}_+ e^{+i\omega_0 t}, \quad \hat{S}'_- = \hat{S}_- e^{-i\omega_0 t}, \qquad (8)$$

the time-dependent part of the Hamiltonian in the interaction picture can be written as

$$\hat{V}'(t) = \hat{V}_z(t) + \sum_{\kappa=\pm} \hat{V}_\kappa(t)e^{i\kappa\omega_0 t}. \qquad (9)$$

Here, the operators

$$\hat{V}_\nu(t) \equiv (b_\nu(t) + \hat{a}_\nu(t))\hat{S}_\nu, \quad \nu = z, \pm , \qquad (10)$$

are defined in terms of the operators

$$\hat{a}_z(t) \equiv \gamma_e \sum_{i=x,y,z} A_{iz}(t)\hat{I}_i,$$

$$\hat{a}_\pm(t) \equiv \gamma_e \sum_i \frac{1}{2}(A_{ix}(t) \mp iA_{iy}(t))\hat{I}_i, \qquad (11)$$

which act only on the nuclear spin state, and the scalars

$$b_z(t) \equiv \gamma_e B_0 G'_{zz}(t),$$

$$b_\pm(t) \equiv \gamma_e B_0 \frac{1}{2}(G'_{zx}(t) \mp iG'_{zy}(t)), \qquad (12)$$

are expressed in terms of the traceless tensor,

$$\mathsf{G}'(t) \equiv \mathsf{G}(t) - G_0\mathsf{E}. \qquad (13)$$

(The symbol E denotes the identity matrix, to distinguish it from the nuclear spin operator $\hat{I}$.)

By going to the interaction picture, the magnitude of the Hamiltonian has been decreased: $\hat{V}_\nu(t)$ are smaller than $\hat{H}(t)$. This leads to variation of $|\psi'(t)\rangle$ on a time scale that is usually longer than the Larmor precession time scale, allowing for the use of a larger integration time step. At the same time, in the rotating frame, parts of the Hamiltonian acquire fast oscillations at the Larmor frequency: The exponents $e^{i\kappa\omega_0 t}$ in Eq. (9). If the magnetic tensors $\mathsf{G}(t)$ and $\mathsf{A}(t)$, and thus, the coefficients $\hat{V}_\nu(t)$, fluctuate on a time scale much slower than the Larmor precession time scale, then these fast fluctuations could average out the effect of the terms $\hat{V}_\pm(t)$. A slowly changing observable, such as the transverse magnetization, can then be calculated by considering only the slowly varying part, $\hat{V}_z(t)$, of the Hamiltonian Eq. (9). This leads to the high-field approximation, to which we now turn.

2. The high-field approximation

Assume that the operators $\hat{V}_\nu(t)$ in Eq. (9) are slowly varying in comparison with the fast time scale of Larmor precession. In this section, we introduce the small parameter $\epsilon = 1/\omega_0$ and perform an expansion of the Schrödinger equation (7) in powers of ϵ. The high-field approximation is

derived as the zeroth order term in the expansion. The first order term is analyzed to assess the range of validity of the approximation.

We seek a solution of Eq. (7) in the form

$$|\psi'(t)\rangle = |\psi^0(t)\rangle + \epsilon \sum_{\kappa=\pm} |\psi^\kappa(t)\rangle e^{i\kappa t/\epsilon}, \qquad (14)$$

where $|\psi^0(t)\rangle$ and $|\psi^\kappa(t)\rangle$ are slowly varying. The goal is to derive an equation of motion for $|\psi^0(t)\rangle$, since the rest of the state vector is averaged out by the fast precession. Substituting Eqs. (14) and (9) into Eq. (7) leads to

$$|\dot{\psi}^0(t)\rangle + \sum_{\kappa=\pm} (\epsilon|\dot{\psi}^\kappa(t)\rangle + i\kappa|\psi^\kappa(t)\rangle)e^{i\kappa t/\epsilon}$$

$$= -i\hat{V}_z(t)|\psi^0(t)\rangle - \epsilon i \sum_{\mu,\kappa=\pm} \hat{V}_{-\mu}(t)|\psi^\kappa(t)\rangle e^{i(\kappa-\mu)t/\epsilon}$$

$$- i\sum_{\kappa=\pm} (\hat{V}_\kappa(t)|\psi^0(t)\rangle - \epsilon\hat{V}_z(t)|\psi^\kappa(t)\rangle)e^{i\kappa t/\epsilon}, \qquad (15)$$

which contains slowly varying terms, proportional to $e^{0t/\epsilon}$, and small terms, proportional to ϵ. By collecting the slowly varying terms only, which survive after time averaging, the desired slow equation of motion is obtained,

$$|\dot{\psi}^0(t)\rangle = -i\hat{V}_z(t)|\psi^0(t)\rangle - \epsilon i \sum_{\kappa=\pm} \hat{V}_{-\kappa}(t)|\psi^\kappa(t)\rangle. \qquad (16)$$

This is an equation for $|\psi^0(t)\rangle$ but it depends on $|\psi^\kappa(t)\rangle$. Since the dependence on $|\psi^\kappa(t)\rangle$ is suppressed by the presence of ϵ, determining these functions to zeroth order in ϵ is enough to have an equation for $|\psi^0(t)\rangle$ correct to the first order in ϵ. Matching the rapidly oscillating terms of order ϵ^0 on both sides of Eq. (15) yields

$$|\psi^\kappa(t)\rangle = -\frac{1}{\kappa}\hat{V}_\kappa(t)|\psi^0(t)\rangle, \qquad (17)$$

to zeroth order in ϵ. Using this approximation in Eq. (16) leads to an equation for the slowly varying part of the state vector, correct to the first order in ϵ,

$$|\dot{\psi}^0(t)\rangle = -i\hat{H}_S(t)|\psi^0(t)\rangle, \qquad (18)$$

where the effective, slow Hamiltonian is

$$\hat{H}_S(t) \equiv \hat{V}_z(t) + \epsilon[\hat{V}_+(t), \hat{V}_-(t)]. \qquad (19)$$

The state vector is of interest only in the context of calculating expectations of Hilbert space operators. Therefore, before proceeding, it is important to check that the expectation values calculated by using $|\psi^0(t)\rangle$ are correct to the first order in ϵ up to time averaging. To the first order, the expectation value of an operator $\hat{O}$ in the interaction picture is

$$\langle\psi'(t)|\hat{O}'|\psi'(t)\rangle = \langle\psi^0(t)|\hat{O}'|\psi^0(t)\rangle$$

$$+ \epsilon \sum_{\kappa=\pm} (\langle\psi^0(t)|\hat{O}'|\psi^\kappa(t)\rangle e^{i\kappa t/\epsilon}$$

$$+ \langle\psi^\kappa(t)|\hat{O}'|\psi^0(t)\rangle e^{-i\kappa t/\epsilon}), \qquad (20)$$

where Eq. (14) was used to write the right hand side of the equality. Indeed, the first order term is oscillatory and van-

TABLE I. Larmor precession frequencies, $f = \omega_e/2\pi$, and associated periods for various magnetic field strengths.

B_0 (T)	0.34	1.21	3.39	6.07	8.92	12.8
f (GHz)	9.5	34	95	170	250	360
T (ps)	100	30	10	6	4	3

ishes after time averaging, indicating that to this order, $|\psi'\rangle$ and $|\psi^0\rangle$ are interchangeable.

Written explicitly, the slow Hamiltonian in Eq. (19) is

$$\hat{H}_S(t) = (b_z(t) + \hat{a}_z(t))\hat{S}_z$$

$$+ \frac{1}{\omega_0}(b_+(t)b_-(t) + b_+(t)\hat{a}_-(t) + b_-(t)\hat{a}_+(t))[\hat{S}_+,\hat{S}_-]$$

$$+ \frac{1}{\omega_0}(\hat{a}_+(t)\hat{a}_-(t)\hat{S}_+\hat{S}_- - \hat{a}_-(t)\hat{a}_+(t)\hat{S}_-\hat{S}_+). \quad (21)$$

The perturbational terms in this expression are suppressed by $1/\omega_0$. To assess their magnitude, let us look at some typical values for the nitroxide magnetic tensors,[31,32]

$$\mathsf{g}^N = \mathrm{diag}(2.008\,09, 2.005\,85, 2.002\,02),$$

$$\mathsf{A}^N = \mathrm{diag}(6.2, 4.3, 36.9) \text{ G}. \quad (22)$$

Since the $b_\pm$ are proportional to the traceless part of g [cf. Eq. (12)], while its trace is proportional to ω_0, the second term on the right hand side of Eq. (21) is about a thousand times smaller than the first term. Similarly, the entries of A are on the order of 30 G, while ω_0 (in units of G) is more than 3 KG at 9 GHz going up to 130 KG at 360 GHz (see Table I), rendering the last term from a hundred to a few thousand times smaller than the first. Neglecting these latter terms and retaining only the $\hat{V}_z$ part of the Hamiltonian are, therefore, justified. This leads to the high-field approximation with effective Hamiltonian

$$\hat{H}_{HF}(t) = \gamma_e(B_0 G'_{zz}(t) + \hat{I}\cdot a(t))\hat{S}_z, \quad (23)$$

where the components of the vector a are defined as

$$a_i(t) \equiv A_{iz}(t). \quad (24)$$

An equivalent form of Eq. (23) is the starting point for the SLE analysis of slow motion for the unsaturated line shapes.[7–13]

The first order terms neglected when going from Eq. (21) to Eq. (23) correspond to double flips of the z component of the electronic spin (as indicated by the presence of $\hat{S}_\pm\hat{S}_\mp$). Thus, what has been neglected is the contribution of spin flips to the decay of the transverse magnetization. Both the slow Hamiltonian Eq. (21) and its zeroth order approximation Eq. (23) are diagonal in the electronic Hilbert space and do not account for the possibility of spin flips. Because the equilibration of the longitudinal magnetization is entirely due to such spin flips, neither of these Hamiltonians can be used when phenomena leading to T_1 relaxation are of interest. In such cases, explicit treatment of the fast dynamics at the time scale of the Larmor precession is necessary.

As a result of the high-field approximation, the spin dynamics of the $m_S = \frac{1}{2}(+)$ and $m_S = -\frac{1}{2}(-)$ sectors of the Hilbert space decouple. This is clearly seen once the state vector

$$|\psi'(t)\rangle = \begin{pmatrix} |\psi'^+(t)\rangle \\ |\psi'^-(t)\rangle \end{pmatrix} \quad (25)$$

and the Hamiltonian (23) are introduced in Eq. (18),

$$\begin{pmatrix} |\dot{\psi}'^+(t)\rangle \\ |\dot{\psi}'^-(t)\rangle \end{pmatrix} = -i\begin{pmatrix} \hat{H}_{HF}^{++}(t) & 0 \\ 0 & \hat{H}_{HF}^{--}(t) \end{pmatrix}\begin{pmatrix} |\psi'^+(t)\rangle \\ |\psi'^-(t)\rangle \end{pmatrix}. \quad (26)$$

(The slow state vector $|\psi^0\rangle$ was replaced by the state vector in the interaction picture $|\psi'\rangle$.) Numerical integration of the quantum dynamics can, therefore, be achieved by separately updating the two parts $|\psi'^\pm\rangle$ of the state vector, according to the short-time propagation scheme,

$$|\psi'^\pm(t+\Delta t)\rangle = e^{\mp i\Delta t\hat{H}_{HF}^{++}(t)}|\psi'^\pm(t)\rangle, \quad (27)$$

where the equality $\hat{H}_{HF}^{--} = -\hat{H}_{HF}^{++}$, valid for the high-field Hamiltonian, was used. The quantum integrator summarized by Eq. (27) is the one used by Eviatar et al.[26] Their vectors P and Q correspond to $|\psi'^\pm\rangle$.

3. The spectrum and the reduced density operator

The FID spectrum, which we aim to simulate, is the Fourier–Laplace transform of the transverse magnetization $M_+ = M_x + iM_y$,

$$\tilde{M}_+(\omega) = \int_0^\infty e^{-i\omega t}M_+(t)dt. \quad (28)$$

Here, $M_+(t) = \langle\hat{M}_+(t)\rangle$ is the quantum mechanical expectation of the operator $\hat{M}_+ \propto \hat{S}_+$. (The proportionality constant is neglected, since the absolute value of the measured spectrum depends on the instrumental factors and is not very relevant.) Two consequences follow from the proportionality of $\hat{M}_+$ to $\hat{S}_+$. First, from Eq. (8), $M_+(t)$ satisfies

$$M_+(t) = \langle\psi'(t)|\hat{M}'_+|\psi'(t)\rangle = e^{i\omega_0 t}\langle\psi'(t)|\hat{M}_+|\psi'(t)\rangle. \quad (29)$$

Therefore, one can sandwich the operator $\hat{M}_+$ in the Schrödinger picture with the state vector in the interaction picture and simply shift the resulting spectrum by the Larmor frequency,

$$\tilde{M}_+(\omega + \omega_0) = \int_0^\infty e^{-i\omega t}\langle\psi'(t)|\hat{M}_+|\psi'(t)\rangle dt. \quad (30)$$

Second, since $\hat{S}_+$ is a raising operator, for the expectation in Eq. (30), one has

$$\langle\psi'(t)|\hat{M}_+|\psi'(t)\rangle = \langle\psi'^+(t)|\hat{M}_+|\psi'^-(t)\rangle. \quad (31)$$

This last equality motivates the introduction of the (reduced) density matrix,

$$\rho'^{-+}(t) \equiv |\psi'^-(t)\rangle\langle\psi'^+(t)|, \quad (32)$$

in terms of which

$$\langle\psi'(t)|\hat{M}_+|\psi'(t)\rangle = \mathrm{Tr}\{\hat{M}_+\rho'^{-+}(t)\}. \quad (33)$$

In the high-field approximation, the dynamics of ρ'^{-+} are decoupled from the dynamics of the other sectors of the spin density matrix [ρ'^{++}, ρ'^{+-}, and ρ'^{--}, analogously defined to Eq. (32)]. From the propagation scheme in Eq. (27) and the definition of ρ'^{-+}, its short-time dynamics automatically follow:

$$\rho'^{-+}(t + \Delta t) = e^{i\Delta t \hat{H}_{HF}^{++}(t)} \rho'^{-+}(t) e^{i\Delta t \hat{H}_{HF}^{++}(t)}. \quad (34)$$

Note that the same matrix acts on both sides of ρ'^{-+} in this last equation, which is different from the propagation of the density matrix in the full Hilbert space.

Equation (34) forms the basis of our integrator for the (relevant sector) of the quantum spin dynamics. Its numerical efficiency depends on the possibility to rapidly calculate the matrix exponential,

$$e^{i\Delta t \hat{H}_{HF}^{++}(t)} = e^{i\Delta t(1/2)\gamma_e(B_0 G'_{zz}(t) + \boldsymbol{a}(t)\cdot\hat{\boldsymbol{I}})}, \quad (35)$$

at each time step. Since the first term in the parentheses leads to a simple, time-dependent phase factor, the problem reduces to the evaluation of the matrix exponential due to the second term. Straightforwardly, this can be achieved by first diagonalizing the matrix $\boldsymbol{a}(t)\cdot\hat{\boldsymbol{I}}$ in the nuclear spin space with a similarity transformation, exponentiating its eigenvalues, and performing the similarity transformation in reverse. A more efficient alternative is possible due to the relation between the nuclear spin matrices and the three dimensional representation of the rotation group.[33] For the latter, it is known that the matrix

$$\hat{N} = \sum_i n_i \hat{I}_i, \quad (36)$$

where $\boldsymbol{n} = (n_x, n_y, n_z)$ is a unit vector, satisfies

$$e^{-i\theta\hat{N}} = \hat{E}_I - i(\sin\theta)\hat{N} - (1 - \cos\theta)\hat{N}^2. \quad (37)$$

Here, to prevent confusion with the nuclear spin operator, $\hat{E}_I$ denotes the identity operator in the three dimensional Hilbert space of the nuclear spin. [Equation (37) can be easily verified by using $\hat{N}^3 = -\hat{N}$.] As a result, solving the eigenvalue problem of $\boldsymbol{a}(t)\cdot\hat{\boldsymbol{I}}$ at each time step is avoided. Instead, the magnitude a and direction $\boldsymbol{n}$ of the vector $\boldsymbol{a}(t)$ are calculated. The rotation angle $\theta = \gamma_e\Delta t\frac{1}{2}a$ and the unit vector $\boldsymbol{n}$ are used to construct the short-time propagator (37), as shown explicitly in Eqs. (A1) and (A2).

At this stage, our choice to perform the quantum propagation by using Eq. (34) instead of Eq. (27) seems to be largely a matter of taste since the same short-time propagator [Eq. (35)] needs to be calculated for both. In fact, when working with ρ'^{-+}, one has to keep track of a 3×3 matrix, whereas only two 3×1 vectors are updated when working with $|\psi'^{\pm}\rangle$. The advantage of the density matrix becomes apparent when the initial conditions of the quantum process are considered.

What we want to simulate is the FID after a $\pi/2$ (90°) pulse applied at time $t=0$. The pulse rotates the macroscopic magnetization to the x-y plane; therefore, right after the pulse, $M_+(t=0^+)=1$. However, this initial condition does not uniquely determine the state vector $|\psi(0^+)\rangle$. Thus, working

with the state vector requires an additional averaging over all the possible starting state vectors that give the correct initial magnetization. In Ref. 34, for example, the entries of the starting state vector were randomly generated subject to the constraint $\langle\psi(0^+)|\hat{S}_+|\psi(0^+)\rangle = 1$. For each of those vectors, the Schrödinger equation was numerically propagated and the results were averaged. The necessity to randomly vary the initial state vector and repeat the calculation disappears if one works with the density matrix, since the latter already represents the ensemble average of all the state vectors consistent with the macroscopic initial condition. Propagating the density matrix, therefore, eliminates the sampling noise associated with averaging over a finite number of random initial state vectors and completely justifies the extra computational cost of propagating a 3×3 matrix as opposed to a 3×1 vector.

At equilibrium, decoupled initial conditions can be assumed for the classical and quantal processes; thus, $\rho(0) = \rho^{eq}$, where the equilibrium density operator is given in terms of the average Hamiltonian,

$$\rho^{eq} \propto \exp(-\hbar\bar{\hat{H}}/k_B T). \quad (38)$$

(Here k_B is Boltzmann's constant and T is temperature.) At room temperature, the average Hamiltonian is typically less than 1% of $k_B T$, so the exponential can be expanded to the first order. For a sample equilibrated under the influence of a constant magnetic field in the z direction,

$$\rho^{eq} \simeq a(\hat{E} - b\hat{S}_z), \quad (39)$$

where $\hat{E}$ is the identity operator in Hilbert space, and a and b are scalar coefficients. At any later time, the density matrix can always be written in the form

$$\rho(t) \simeq a(\hat{E} + \sigma(t)), \quad (40)$$

since $\hat{E}$ commutes with the Hamiltonian. Additionally, $\hat{E}$ has no effect on the expectation value of the magnetization, $\text{Tr}\{\hat{\boldsymbol{M}}\hat{E}\} = 0$, because $\hat{\boldsymbol{M}}$ is proportional to $\hat{\boldsymbol{S}}$. As a result, one only needs to keep track of $\sigma(t)$, which in that sense is the relevant part of the density matrix. From Eq. (39), $\sigma(0) = \sigma^{eq} \propto \hat{S}_z$. After the 90° pulse, $\sigma(0^+) \propto \hat{S}_y$, which implies that $\sigma^{-+}(0^+) \propto \hat{E}_I$.

B. Generating stochastic trajectories for rotational diffusion

In this section, we develop an efficient numerical integrator for the rotational Brownian diffusion of a body-fixed frame B with respect to a space-fixed frame S. The presence of an ordering potential $U(\Omega)$, where $\Omega = \{\alpha, \beta, \gamma\}$ denotes the instantaneous orientation of B with respect to S parametrized by using the Euler angles α, β, and γ, is also allowed. This basic model forms the basis for more sophisticated motional models such as MOMD and SRLS.

1. Quaternions and rotational dynamics

When dealing with kinematics of rotations, it is more convenient to work with quaternions rather than Euler angles

[The relation between the two sets of parameters is given in Eq. (B1).] To keep track of the orientation of B with respect to S, we use the 2×2 unitary matrices,

$$\mathcal{Q} = \begin{pmatrix} q_0 - iq_3 & -q_2 - iq_1 \\ q_2 - iq_1 & q_0 + iq_3 \end{pmatrix} = q_0 \sigma_0 - i \sum_i q_i \sigma_i, \qquad (41)$$

with unit determinant,

$$q_0^2 + q_1^2 + q_2^2 + q_3^2 = 1. \qquad (42)$$

The Pauli spin matrices σ_1, σ_2, and σ_3 and the 2×2 identity matrix σ_0 should not be confused with the density matrix of the previous section. The real numbers q_i are the components of the quaternion corresponding to the transformation relating B to S. When the coordinate frame B moves with respect to S, $\mathcal{Q}$ becomes time dependent. Its equation of motion is

$$\frac{d}{dt} \mathcal{Q}(t) = \mathcal{W}(t) \mathcal{Q}(t), \qquad (43)$$

where

$$\mathcal{W}(t) = -i \frac{1}{2} \sum_i \omega_i(t) \sigma_i. \qquad (44)$$

In these expressions, $\boldsymbol{\omega}(t)$ is the instantaneous angular velocity of B. Its components ω_i are with respect to S. Given a time series of $\boldsymbol{\omega}(t)$, Eq. (43) can be numerically integrated to generate the time series of $\mathcal{Q}$, as was done by Fedchenia *et al.* in their rigorous treatment of isotropic rotational diffusion restricted to a conical region.[28]

In the case of anisotropic diffusion, it becomes necessary to work with the components of $\boldsymbol{\omega}$ with respect to B (will be discussed in more detail below). Denoting these by $\omega_{i'}$ and defining

$$\mathcal{W}_r(t) = -i \frac{1}{2} \sum_i \omega_{i'}(t) \sigma_i, \qquad (45)$$

the equation of motion of $\mathcal{Q}$ becomes

$$\frac{d}{dt} \mathcal{Q}(t) = \mathcal{Q}(t) \mathcal{W}_r(t). \qquad (46)$$

(The prime as a subscript should not be confused with the prime as a superscript, which was used to denote states and operators in the interaction picture.) Observe the algebraically trivial but important difference between Eqs. (43) and (46). In the former, the components of the angular velocity of the rotating frame are with respect to the stationary frame; in the latter, they are with respect to the body-fixed frame. Equation (46) may be integrated numerically as

$$\mathcal{Q}(t + \Delta t) = \mathcal{Q}(t) e^{\Delta t \mathcal{W}_r(t)}. \qquad (47)$$

This form of propagation is very attractive because it preserves the determinant of $\mathcal{Q}$ and, thus, the normalization of the quaternion [Eq. (42)]. In close similarity to the evaluation of Eq. (35) by using Eq. (37), the matrix in Eq. (47) can be exponentiated calculating only trigonometric functions,

$$\exp\left(-i \sum_i \frac{\omega_{i'}(t) \Delta t}{2} \sigma_i \right)$$

$$= \cos\theta \sigma_0 - i \sin\theta \sum_i u_i \sigma_i$$

$$= \begin{pmatrix} \cos\theta - iu_z \sin\theta & -(u_y + iu_x)\sin\theta \\ (u_y - iu_x)\sin\theta & \cos\theta + iu_z \sin\theta \end{pmatrix}. \qquad (48)$$

Here, θ and $\underline{u} = (u_x, u_y, u_z)$ denote, respectively, the magnitude and the direction of the vector $\boldsymbol{\omega}'(t) \Delta t / 2$. Equations (47) and (48) constitute our numerical scheme for propagating the quaternion $\mathcal{Q}_{SB}$ describing the orientation of the coordinate system B with respect to the system S. What is missing so far is the physics of the orientational dynamics, to be addressed next, which determines how $\boldsymbol{\omega}'(t)$ changes with time.

2. Anisotropic Brownian diffusion in external potential

Starting from this section, we drop the subscript prime with the understanding that all the vector and tensor components are with respect to B. We are interested in describing rotational diffusion in the presence of a potential $U(\Omega)$. In the limit of high friction, when inertial terms can be neglected, the components of the instantaneous angular velocity $\boldsymbol{\omega}(t)$ (in B) satisfy the equation of motion,[35,36]

$$\boldsymbol{\omega}(t) = -\mathsf{D} \boldsymbol{\nabla} u(\Omega(t)) + \boldsymbol{\xi}(t). \qquad (49)$$

The first term on the right hand side of the equality corresponds to the systematic torque due to the potential

$$u(\Omega) \equiv U(\Omega)/k_B T, \qquad (50)$$

whereas the second term is the random torque which leads to the orientational diffusion. The other symbols in Eq. (49) are the rotational diffusion tensor D (diagonal in B) and the orientational gradient operator,[33]

$$\boldsymbol{\nabla} = \left(\frac{\partial}{\partial \phi_x}, \frac{\partial}{\partial \phi_y}, \frac{\partial}{\partial \phi_z} \right), \qquad (51)$$

where ϕ_i is the angle of rotation around the ith axis of B. The components of the random torque satisfy the conditions[35,36]

$$\mathbb{E}\{\xi_i(t)\} = 0, \quad \mathbb{E}\{\xi_i(t_1)\xi_j(t_2)\} = 2D_{ii}\delta_{ij}\delta(t_1 - t_2), \qquad (52)$$

where $\mathbb{E}$ denotes expectation over the Gaussian probability density of $\boldsymbol{\xi}$. In this last expression, D_{ii} are the components of D (with respect to B).

It is important to realize that conditions (52) are valid only when the components of $\boldsymbol{\xi}$ are with respect to the coordinate frame in which the diffusion tensor is diagonal. Only in this frame do the components of the diffusion tensor and, therefore, the intensities of the random torque decouple. An isotropic diffusion tensor is diagonal in any coordinate system, including the space-fixed frame, which makes it possible to exclusively express all the vector components with respect to S. To treat the general anisotropic case, we have to work with the components of the diffusion tensor with respect to B. Hence, as already alluded to, using Eq. (46) instead of Eq. (43) is crucial.

By writing the torque $-\nabla u(\Omega)$ in terms of the angular momentum operator $\mathbf{J}$,[10,35,36]

$$-\nabla u(\Omega) = -i\mathbf{J}u(\Omega), \tag{53}$$

Equation (49) can be rewritten in component form as

$$\omega_i(t) = -iD_{ii}J_i u(\Omega(t)) + \xi_i(t), \tag{54}$$

where the partial differential operators corresponding to the components J_i (in B) are[37]

$$
\begin{aligned}
J_z &= -i\frac{\partial}{\partial\gamma} \\
J_{\pm} &= e^{\mp i\gamma}\left[-i\cot\beta\frac{\partial}{\partial\gamma} \pm \frac{\partial}{\partial\beta} + \frac{i}{\sin\beta}\frac{\partial}{\partial\alpha}\right],
\end{aligned} \tag{55}
$$

with $J_{\pm} = J_x \pm iJ_y$. The action of the J_i on the potential becomes analytically tractable if the latter is written as an expansion over the eigenfunctions of the former. The Wigner functions,

$$\mathcal{D}_{nm}^j(\Omega) = e^{-in\alpha}d_{nm}^j(\beta)e^{-im\gamma}, \tag{56}$$

are eigenfunctions of J_z that satisfy[37]

$$
\begin{aligned}
J_z\mathcal{D}_{nm}^j(\Omega) &= -m\mathcal{D}_{nm}^j(\Omega), \\
J_{\pm}\mathcal{D}_{nm}^j(\Omega) &= -\sqrt{j(j+1)-m(m\pm1)}\mathcal{D}_{nm\pm1}^j(\Omega).
\end{aligned} \tag{57}
$$

Therefore, it is convenient to choose the ordering potential in the form[8–12]

$$u(\Omega) = -\sum_{j,m}c_m^j\mathcal{D}_{0m}^j(\Omega), \tag{58}$$

which leads to the expressions

$$
\begin{aligned}
-iJ_x u &= -\frac{i}{2}\sum_{j,m}c_m^j(C_+^{j,m}\mathcal{D}_{0m+1}^j + C_-^{j,m}\mathcal{D}_{0m-1}^j), \\
-iJ_y u &= -\frac{1}{2}\sum_{j,m}c_m^j(C_+^{j,m}\mathcal{D}_{0m+1}^j - C_-^{j,m}\mathcal{D}_{0m-1}^j), \\
-iJ_z u &= -i\sum_{j,m}c_m^j m\mathcal{D}_{0m}^j,
\end{aligned} \tag{59}
$$

where the coefficients,

$$C_{\pm}^{j,m} \equiv \sqrt{j(j+1)-m(m\pm1)}, \tag{60}$$

have been introduced to simplify the notation. Expressions (59) are evaluated in Appendix C for some popular choices of the potential. There, the advantage of writing the differential operator (51) in terms of the angular momentum operators J_i becomes apparent. The action of J_z and $J_{\pm}$ on the Wigner rotation matrices transforms the problem of differentiation of the potential to straightforward algebraic manipulation of the components of the corresponding quaternion. The only remaining task is to account for the random term in Eq. (54). Given its statistical properties [Eq. (52)], the numerical integration of Eq. (54) involves the generation of three random numbers $N_i(t)$ with Gaussian distribution of zero mean and unit standard deviation, which are then used to calculate

$$\frac{\omega_i(t)\Delta t}{2} = -iJ_i u(\mathcal{Q}(t))\frac{D_{ii}\Delta t}{2} + \sqrt{\frac{D_{ii}\Delta t}{2}}N_i(t). \tag{61}$$

The combination $\omega_i(t)\Delta t/2$ was the necessary input to Eqs. (47) and (48).

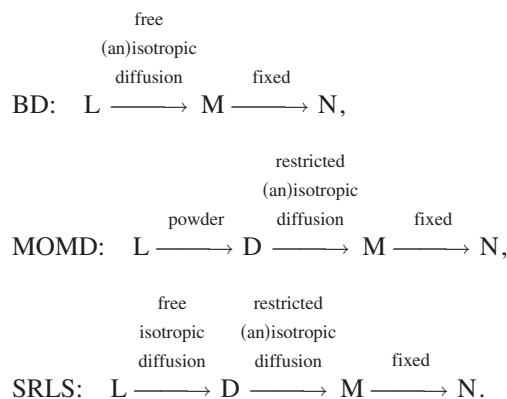### 3. Spherical grid for the initial conditions

Finally, we consider the initial conditions for the rotational diffusion, which can be generated as random orientations of B with respect to S, weighted by the Boltzmann factor $\exp(-u(\Omega))$. In practice, systematically covering the surface of a sphere with a homogeneously distributed grid is found to be much more efficient than a random choice.[38] Different spherical grids are compared in Ref. 38, where it is conclusively demonstrated that distributing the points along a spiral that twists from the north pole to the south pole leads to the most efficient grid with high convergence rate. The spherical polar coordinates of the points along the spiral are[38]

$$\theta_i = \arccos(s_i), \quad \phi_i = \sqrt{\pi N}\arcsin(s_i), \tag{62}$$

where $s_i \in (-1,1), i = 1, \ldots, N$, parametrizes the spiral and N is the number of points on the spiral. The potentials $u(\Omega)$ that we consider are proportional to $\mathcal{D}_{0m}^j(\Omega)$ (see Appendix C). Since these Wigner functions are independent of α, the initial conditions for the Euler angles are chosen as $\alpha = 0$, $\beta = \theta_i$, and $\gamma = \phi_i$, and the corresponding quaternion is calculated by using Eq. (B1).

C. Testing the integrators

By building on the rotational dynamics discussed above, it is straightforward to generate trajectories for typical stochastic models of the spin label dynamics such as Brownian rotational diffusion (BD), MOMD[9] and SRLS,[10,11] which schematically can be represented as

$$
\text{BD:} \quad L \xrightarrow[\substack{\text{free} \\ \text{(an)isotropic} \\ \text{diffusion}}]{} M \xrightarrow[\text{fixed}]{} N,
$$

$$
\text{MOMD:} \quad L \xrightarrow[\text{powder}]{} D \xrightarrow[\substack{\text{restricted} \\ \text{(an)isotropic} \\ \text{diffusion}}]{} M \xrightarrow[\text{fixed}]{} N,
$$

$$
\text{SRLS:} \quad L \xrightarrow[\substack{\text{free} \\ \text{isotropic} \\ \text{diffusion}}]{} D \xrightarrow[\substack{\text{restricted} \\ \text{(an)isotropic} \\ \text{diffusion}}]{} M \xrightarrow[\text{fixed}]{} N.
$$

In the last two models, the molecular frame M is allowed to diffuse with respect to D. The ordering potential which restricts the diffusion of M is fixed in this latter "director" frame. In that sense, M and D correspond, respectively, to the body-fixed frame B and stationary frame S of Sec. II B. D itself can be either randomly oriented (MOMD) or undergo free isotropic diffusion (SRLS) with respect to L.
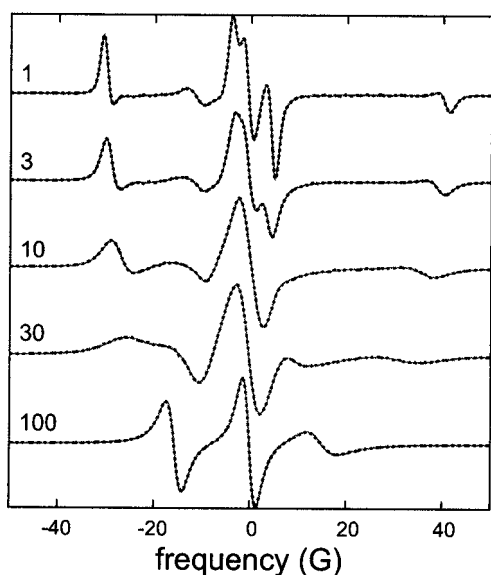
FIG. 1. Spectra of isotropic-free diffusion for various diffusion rates in units of 10^6 s^{-1} (indicated next to each spectrum), simulated by using the trajectory-based approach (dashed lines) and the SLE (continuous lines). The magnetic tensors g^N and A^N are given in Eq. (22); $B_0 = 0.34$ T.

When treating the diffusive motion of D with respect to L, the former plays the role of the body-fixed frame B and the latter of the stationary frame S. In the BD model, there is no ordering potential; thus, the intermediate director frame is skipped. To simulate this model by using the formalism of Sec. II B, L is identified with S and M with B. The initial conditions for each of the diffusion parts in a given model are chosen from points distributed on a spherical grid.

In addition to the dynamical events explicitly present in the models, the spectral lines are typically broadened due to relaxation mechanisms not accounted for in the simulation. Such broadening can be easily included phenomenologically in the form of Lorentzian and Gaussian relaxation times. Lorentzian broadening with relaxation time constant T_L is achieved by multiplying the magnetization $M_+(t)$ by e^{-t/T_L}. Gaussian broadening is introduced by convoluting the spectral lines with a Gaussian. Since convolution in the frequency domain is multiplication in the time domain, this can be done by multiplying $M_+(t)$ by $e^{-t^2/8T_G^2}$, where T_G is the derivative peak-to-peak linewidth of the Gaussian. Last, the trajectories are of some finite duration T. To prevent the contamination of the spectrum with high frequencies due to the abrupt termination of the trajectories, the integrand is multiplied by the Hamming window,[39]

$$h_T(t) = 0.54 + 0.46 \cos(\pi t/T). \quad (63)$$

An absorption spectrum in derivative mode is, therefore, calculated as

$$\frac{d\tilde{M}_+(\omega)}{d\omega} = \mathrm{Im} \int_0^T dt\, t e^{-i\omega t} h_T(t) e^{-t/T_L} e^{-t^2/8T_G^2} M_+(t). \quad (64)$$

ESR spectra at $B_0 = 0.34$ T for the BD model with isotropic diffusion are presented in Fig. 1. Our time-domain spectra, simulated by using the proposed trajectory-based approach, are compared with spectra simulated by using the

TABLE II. Time scales, $\tau = 1/6D$, for the diffusion rates used in the simulation of the spectra in Figs. 1–3.

D ($\times 10^6$ s^{-1})	1	3	10	30	100
τ (ns)	167	55.6	16.7	5.56	1.67

SLE-based software of Freed and co-workers over motional regimes ranging from slow ($D = 1 \times 10^6$ s^{-1}) to fast ($D = 100 \times 10^6$ s^{-1}). The correlation time scales associated with these diffusion rates range from 1.67 to 167 ns (Table II). Excellent agreement between the two simulation strategies is observed over the whole motional regime. The effect of the anisotropy of the diffusion tensor is illustrated in Fig. 2, where spectra simulated by using trajectories are superimposed with spectra simulated with the SLE. Again, the agreement is excellent. As expected, fast rotational diffusion about the nitroxide z axis ($D_{zz} > D_{yy} > D_{xx}$, top spectrum) does not mix the larger A_{zz} component with the smaller A_{xx} and A_{yy} components as efficiently as fast rotation about the x and y axes (bottom two spectra). Therefore, the resulting spectrum is more slowlike in the former case compared to the latter two, for which the averaging of A_{zz} is more efficient. Figure 3 illustrates the effect of the ordering potential on the spectra. The ordering potential for the top spectrum was as given in Eq. (C7) with $c_0^2 = 2.0$. The potential for the bottom spectrum was as in Eq. (C9) with $c_2^2 = 2.0$. Isotropic diffusion with $D = 30 \times 10^6$ s^{-1} was used for both of the simulations. Again, the continuous lines were simulated in the frequency domain, by the SLE, and the dashed lines in the time domain. The agreement is excellent.

The values of the magnetic tensors used in the simulations in Figs. 1–3 are given in Eq. (22). The other simulation parameters are summarized in Table III. There, "stpN" indicates the number of simulation steps that each stochastic trajectory lasted and Δt is the integration time step. Naturally, the duration of each trajectory is the product of these two. "freN" and "rstN" are the numbers of spherical grid points used for the two separate spherical grids. freN points were used for the free diffusion of M (BD) and the random distri-
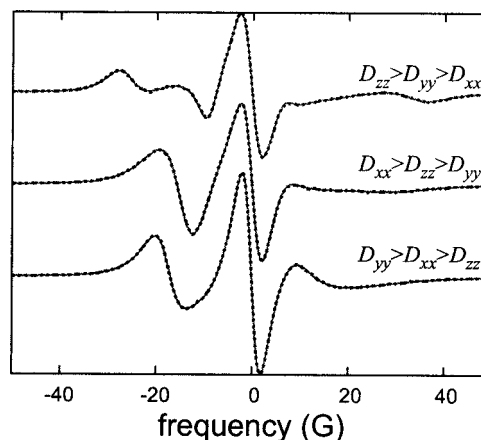

FIG. 2. Simulated time-domain (dashed) and frequency-domain (continuous) spectra of anisotropic-free diffusion. The components of the diffusion tensor, $10\times$, $30\times$, and 100×10^6 s^{-1}, were assigned in the order indicated in the plot. The magnetic tensors are given in Eq. (22); $B_0 = 0.34$ T.
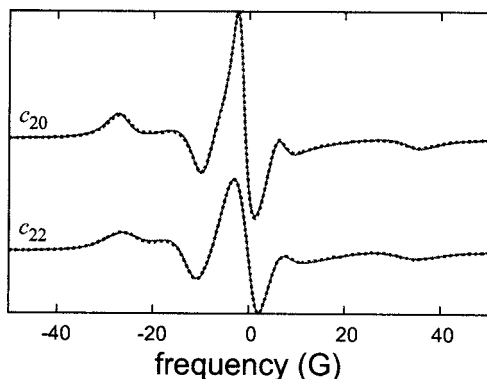
FIG. 3. Comparison of time-domain (dashed) and SLE (continuous) spectra for two MOMD models with $(c_0^2, c_2^2) = (2.0, 0)$ and $(0, 2.0)$, respectively. The nonzero coefficient is indicated next to the spectrum. $D = 30 \times 10^6$ s^{-1}. The magnetic tensors are given in Eq. (22); $B_0 = 0.34$ T.

bution of D (MOMD) with respect to L. rstN points were used for the restricted diffusion of M with respect to D (MOMD). Since this last diffusion is not present in the BD model, rstN in this case indicates the number of independent trajectories initiated from each of the freN spherical grid points. Finally, the last column gives the value of the inhomogeneous Gaussian broadening introduced in the spectra by hand. Note that the integration time step used to simulate the spectra in Figs. 1 and 2 is much smaller than the correlation time scales of the rotational diffusion (Table II); thus, it should be sufficient to follow the dynamics. The only exception is $D = 100 \times 10^6$ s^{-1}. The excellent agreement of our spectra with the spectra simulated by using the SLE indicates that even in this case, the integration time step is adequate. A smaller integration time step was chosen for the two MOMD models to ensure the faithful resolution of the gradient of the potential energy.

To the best of our knowledge, this is the first time that ESR spectra simulated by using trajectories of free or restricted nonisotropic rotational diffusion models show quantitative agreement with spectra simulated by using the SLE.[40] It is worth emphasizing though, that the simulation of the spectra reported in Figs. 1–3 by using stochastic trajectories took at least a thousand times more computer time than their calculation with the SLE. Using trajectories is, therefore, justified only when the dynamics is not amenable to treatment with the SLE, as in the case of MD simulations. When spectra of the BD, MOMD, and SRLS models need to be simulated, the SLE is much more efficient and should be the method of choice.

III. COMBINING MD AND STOCHASTIC TRAJECTORIES

MD simulations of a spin labeled macromolecule are expected to offer insight into the detailed dynamics of the

TABLE III. Parameters used in the simulation of the spectra in Figs. 1–3.

Model	B_0 (T)	stpN	Δt (ns)	freN	rstN	T_G^{-1} (G)
BD	0.34	800	1.0	1600	800	1.0
MOMD	0.34	2000	0.4	3200	1600	1.0

spin label and its environment. At the same time, the simulations will most certainly fail to sample the global macromolecular dynamics, e.g., the tumbling of a protein in solution. In such cases, the MD trajectories will not realistically reflect the experimental situation and ESR spectra simulated from them will fail to reproduce the observed spectra. Thus, for the quantitative comparison of simulated and recorded spectra, it becomes necessary to be able to introduce the effect of the rotational diffusive dynamics in addition to the dynamics of the spin label present in the MD trajectories. This can be achieved by allowing the coordinate system M, attached to the macromolecule, to undergo isotropic (or anisotropic) rotational diffusion with respect to the laboratory-fixed coordinate frame L,

$$
\begin{array}{ccc}
\text{rotational} & & \text{MD} \\
\text{diffusion} & & \text{trajectories} \\
L \xrightarrow{\hspace{1cm}} & M & \xrightarrow{\hspace{1cm}} N.
\end{array}
\qquad (65)
$$

In this scheme, the dynamics of the coordinate frame N with respect to M are provided by the MD trajectories, whereas the dynamics of M with respect to L are generated by using the time-domain formalism developed in the previous section. Below, we will discuss a few formal issues related to putting such a stochastic/MD trajectory-based approach into use and illustrate its application by using the MD trajectories of a spin labeled, polyalanine α helix in explicit solvent.[25]

A. Coarse graining the MD trajectories in time

The trajectories coming from atomistic MD simulations are typically sampled about every $\delta t = 1$ ps.[25] Although it is possible to use every snapshot from the trajectories and integrate the quantum spin dynamics with this time step, this would be wasteful since the magnetization relaxes on a much longer time scale. One option is to decimate the MD trajectories and use snapshots separated by a hundred or a thousand steps. Alternatively, the magnetic tensors can be averaged over a time window Δt ($\Delta t \gg \delta t$), along each MD trajectory. The time averaging can be justified by the same arguments that led to the high-field approximation. The only complication is the possibility of resonance[41,42] between the Larmor precession and the variations of the magnetic tensors at the Larmor frequency. Eventually, we will neglect the effect of the resonance but to clarify the assumptions making this possible, we start by considering it.

The Fourier series decomposition of the operators $\hat{V}_{\kappa = z, \pm}(t)$, defined in Eq. (10), in the interval $[t, t + \Delta t]$ can be written as

$$
\hat{V}_\kappa(t + \tau) = \hat{V}_\kappa^{(0)}(t) + \sum_{\mu \neq 0} \hat{V}_\kappa^{(\mu)}(t) e^{i\mu\tau/\epsilon},
\qquad (66)
$$

where $\tau \in [0, \Delta t)$, $\epsilon = \Delta t / 2\pi$, and $\mu = \pm 1, \pm 2, \ldots$. The zero-frequency term $\hat{V}_\kappa^{(0)}(t)$ has been separated from the fast fluctuations which are isolated in the exponents $e^{i\mu\tau/\epsilon}$. The coefficients $\hat{V}_\kappa^{(\nu)}(t)$ are slowly varying. They are constant during each time interval Δt and change only when going from one interval to the next, which is the reason for their t dependence. The part $\hat{V}_\kappa^{(0)}(t)$ is the average value of the

Hamiltonian in each time interval; it is the only part that we will ultimately use.

To simplify the argument and keep track of the resonance, let us choose the fast time scale, over which we intend to average, to be an integer multiple of the Larmor precession time scale: $\epsilon = n/\omega_0$. With that, the interaction Hamiltonian becomes

$$\hat{V}'(t) = \hat{V}^{(0)}(t) + \sum_{\mu \neq 0} \hat{V}^{(\mu)}(t) e^{i\mu t/\epsilon}, \tag{67}$$

where we have defined

$$\hat{V}^{(\nu)}(t) \equiv \hat{V}_z^{(\nu)}(t) + \sum_{\kappa = \pm} \hat{V}_\kappa^{(\nu - \kappa n)}(t) \tag{68}$$

for $\nu = 0, \pm 1, \pm 2, \ldots$ [cf. Eq. (9)]. As before, we look for a solution of the Schrödinger equation (7) in the form (14). Again, our goal is to derive an equation of motion for $|\psi^0(t)\rangle$ only, since the fast oscillations will average out the rest. The nonoscillating terms give

$$|\dot{\psi}^0(t)\rangle = - i\hat{V}^{(0)}(t)|\psi^0(t)\rangle - \epsilon i \sum_{\mu \neq 0} \hat{V}^{(-\mu)}(t)|\psi^\mu(t)\rangle, \tag{69}$$

whereas the oscillating terms, proportional to $e^{i\mu t/\epsilon}$ with $\mu \neq 0$, lead to

$$i\mu|\psi^\mu(t)\rangle + \epsilon|\dot{\psi}^\mu(t)\rangle = - i\hat{V}^{(\mu)}(t)|\psi^0(t)\rangle$$
$$- \epsilon i \sum_{\nu \neq 0} \hat{V}^{(\mu - \nu)}(t)|\psi^\nu(t)\rangle. \tag{70}$$

When an equation for $|\psi^0(t)\rangle$ to the first order in ϵ is desired, it is enough to determine $|\psi^\mu(t)\rangle$ to zeroth order in ϵ from this last equation. To that order,

$$|\psi^\mu(t)\rangle = - \frac{1}{\mu}\hat{V}^{(\mu)}(t)|\psi^0(t)\rangle. \tag{71}$$

By substituting in Eq. (69), we obtain

$$|\dot{\psi}^0(t)\rangle = - i\hat{H}_S(t)|\psi^0(t)\rangle, \tag{72}$$

with slow Hamiltonian

$$\hat{H}_S(t) \equiv \hat{V}^{(0)}(t) + \epsilon \sum_{\mu > 0} \frac{1}{\mu}[\hat{V}^{(\mu)}(t), \hat{V}^{(-\mu)}(t)]. \tag{73}$$

Equation (73) is a generalization of Eq. (19). There, to zeroth order, one only had to consider $\hat{V}_z(t)$, which was proportional to $\hat{S}_z$, leading to the slow Hamiltonian Eq. (23). Here, even to zeroth order, terms proportional to $\hat{S}_\pm$, namely, $\hat{V}_\pm^{(\mp n)}(t)$, are present in $\hat{V}^{(0)}(t)$ [as can be seen from Eq. (68) with $\nu = 0$]. As a reminder, n was chosen to be the ratio between the Larmor precession frequency and the frequency for which the time averaging is performed. The terms $\hat{V}_\pm^{(\mp n)}(t)$, therefore, correspond to fast variation in the magnetic tensors at the Larmor frequency. By going to the frame rotating at the Larmor frequency, the oscillations of the magnetic tensors which rotate at the same frequency but in the "opposite sense" are seen at zero frequency. This is the resonance phenomenon that was previously mentioned. We assume that the variation of the magnetic tensors at the time

TABLE IV. Estimates for the duration of the time-averaging window Δt for various magnetic field strengths B_0.

B_0 (T)	0.34	1.21	3.39	6.07	8.92	12.8
Δt (ns)	1	1	1/3	1/5	1/8	1/10

scale of the Larmor frequency is much smaller than the variation during the the time interval Δt over which the averaging is performed. This assumption seems to be reasonable given that the fast time scale (last row of Table I) and the slow time scale (last row of Table IV, to be estimated below) are separated by at least an order of magnitude. Thus, we neglect $\hat{V}_\pm^{(\mp n)}(t)$ in comparison with $\hat{V}_z(t)$. It is worth emphasizing again that neglecting the parts of the Hamiltonian which oscillate on the time scale of the Larmor precession limits our analysis to T_2 relaxation processes. The relaxation of the longitudinal magnetization is driven by $\hat{V}_\pm^{(\mp n)}(t)$ and is entirely missed when these terms are neglected.

Now, let us estimate the magnitude of the correction to the zeroth order slow Hamiltonian. In Eq. (73), $1/\epsilon = 2\pi/\Delta t$, where Δt is the time window over which we want to average. $\Delta t = 1$ ns, for example, corresponds to $f = 1000$ MHz. Variation of A on the order of 30 G is about 100 MHz. Therefore the $\mu = 1$ term containing the hyperfine tensor is suppressed by at least $1/10$. For $B_0 = 1.2$ T, the variation of the traceless part of g is also about 100 MHz and increases for higher fields. Thus $\Delta t = 1$ ns is a conservative time step for $B_0 = 0.34$ and 1.21 T. When $B_0 = 12.8$ T, the time step should be ten times smaller, so $\Delta t = 1/10$ ns is more appropriate. In between, one can choose $\Delta t = 1/3$ ns for $B_0 = 3.4$ T, $\Delta t = 1/5$ ns for $B_0 = 6.07$ T, and $\Delta t = 1/8$ ns for $B_0 = 8.92$ T. These choices are summarized in Table IV. They are on the conservative side, especially for the stronger fields, since we have assumed that the magnetic tensors change by the maximum possible amount over the duration of the averaging interval Δt.

B. Averaged magnetic tensors

Finally, we discuss how to average the magnetic tensors over the desired time interval Δt. The tensors G and A, collectively denoted by T, are diagonal in N. Their transformation to L is achieved as

$$T_{ij}^L(t) = \sum_k R_{ik}(\mathcal{Q}_{LN}(t)) T_{kk}^N R_{jk}(\mathcal{Q}_{LN}(t)), \tag{74}$$

where the rotation matrix $R(\mathcal{Q}_{LN}(t))$ rotates the axes of L to the axes of N at time t. [Equation (B2) shows how the rotation matrix is calculated from the quaternion.] When nested rotational frames are considered,

$$L \xrightarrow{\mathcal{Q}_{LM}(t)} M \xrightarrow{\mathcal{Q}_{MN}(t)} N, \tag{75}$$

the quaternion corresponding to the transformation $L \rightarrow N$ is obtained as the product of the quaternions of all the successive transformations: $\mathcal{Q}_{LN}(t) = \mathcal{Q}_{LM}(t)\mathcal{Q}_{MN}(t)$. Suppose that the last of these transformations is available as a MD trajectory with fine temporal resolution δt. Assuming that the other

TABLE V. Parameters used in the simulation of the spectra in Fig. 4. A lag time of 2.0 ns and an additional Lorentzian broadening of $T_D^{-1}=0.3$ G were used for all the simulations.

B_0 (T)	A		B			
	Δt (ns)	avgN	Δt (ns)	avgN	sphN	T_G^{-1} (G)
0.34	500	200	2.0	800	400	1.0
1.21	500	200	2.0	800	400	1.0
3.39	125	50	0.5	200	3 200	1.5
6.07	100	40	0.4	160	6 400	1.8
8.92	62.5	25	0.25	100	12 800	2.0

transformations evolve on a time scale Δt much longer than δt, the time averaging of the trajectory is performed as follows. First, the averaged magnetic tensors,

$$\overline{\mathsf{T}}^M(t) \equiv \overline{\mathsf{R}_{MN}(t)\mathsf{T}^N\mathsf{R}_{MN}^{\mathsf{T}}(t)}, \qquad (76)$$

are calculated, where the line indicates that the quantity under it is averaged over a time window Δt. Then, for each time window, the coordinate frame in which the averaged tensor is diagonal is determined. The similarity transformation,

$$\overline{\mathsf{T}}^M(t) = \mathsf{R}_{MT}(t)\overline{\mathsf{T}}^{\mathsf{T}}(t)\mathsf{R}_{MT}^{\mathsf{T}}(t), \qquad (77)$$

where $\overline{\mathsf{T}}^{\mathsf{T}}$ is a diagonal matrix, defines the (instantaneous) coordinate frame T of the averaged magnetic tensor. It is clear that, even though G and A are diagonal in the same coordinate frame N, the principle axes of the two frames may generally differ after the averaging. Therefore, one needs to keep track of the frames G and A as a function of the averaging window. This is done by recording the three diagonal entries of $\overline{\mathsf{T}}^{\mathsf{T}}$ (T=G,A) and the quaternion $\mathcal{Q}_{MT}$ (T=G,A) for each averaging window.

C. Application to the spin label side chain R1 attached to a polyalanine α helix

We illustrate the stochastic/MD methodology presented above by using a set of 18 MD trajectories of a spin labeled, 15-residue, polyalanine α helix.[25] The system was fully solvated with 686 TIP3P waters and simulated with CHARMM.[43] The resulting system of 2247 atoms filled a tetragonal simulation box with starting side lengths of 26.0, 26.0, and 34.0 Å. Periodic boundary conditions were used. The electrostatics were treated with particle mesh Ewald summation.[44,45] Pressure and temperature pistons were used to achieve a NpT ensemble at $T=297$ K and $p=1$ atm.[46] To prevent the unfolding of the helix in water, the first five and the last five residues were harmonically restrained to their starting positions with force constants of 0.5 kcal/mol Å^2. Each of the 18 trajectories extended for 100 ns. Snapshots were saved every 1 ps. Additional details about the simulations are given elsewhere.[25]

The effective viscosity of the TIP3P water model used in the simulations is about 2.86 times smaller than the experimental value.[47,48] As a result, the diffusion coefficient of small solutes and molecular moieties tend to be too fast. Since the spin label in the simulations is solvent exposed, we scale the MD time axis by a factor of 2.5 to account for the

underestimated solvent viscosity. Thus, the time interval between two MD snapshots becomes $\delta t=2.5$ ps, and the effective duration of the trajectories becomes 250 ns.

Dividing the estimates of Δt from Table IV by δt gives the number of MD frames one needs to average over. To assess the reliability of the estimated averaging windows, we perform the spectral simulations for two different values of Δt: Half and twice the estimated value. These are listed in Table V as parameter sets A and B, respectively. The numbers in the "avgN" column correspond to the number of δt =2.5 ps steps one averages over to obtain the coarse-grained time step in the Δt column. The last two columns in Table V list the number of spherical grid points "sphN," used to start the stochastic trajectories of isotropic diffusion, and the Gaussian broadening T_G^{-1} introduced in the calculation of the spectra.

The increase in sphN with B_0 in Table V indicates that to achieve a similarly low intensity of the noise in the calculated spectra, one has to average over many more realizations of the dynamics (i.e., trajectories) at higher fields than at lower fields. This is related to the fact that high-field spectra are much more sensitive to the details of the dynamics, as evident from the progressive shortening of the estimated averaging window Δt (Table IV). A similar demand on the number of realizations applies to the MD trajectories when they are used to simulate ESR spectra. Not surprisingly, the spectra for $B_0 \geqslant 3.4$ T, calculated according to the model [Eq. (65)] by using the 18 MD trajectories as is, are unacceptably noisy (not shown). The problem is significantly alleviated by using the valuable dynamical information present in the MD trajectories in a less wasteful way. Whereas the $\pi/2$ pulse fixes the origin of time for the quantal dynamics of the spins, the classical dynamics of the spin label is not affected by it and is invariant under translation of the time axis. Therefore, we can imagine that the pulse is applied when the MD trajectories have already progressed up to some arbitrary time t and simulate the free induction decay by using the remaining part of the trajectories. More systematically, we use one MD trajectory several times by starting from time instances separated by a fixed lag time. For convenience, we choose the lag time to be the same as the largest averaging window in Table V, namely, 2 ns. As a result, each MD trajectory (with duration of 250 ns after scaling by 2.5) is used 125 times, but the additional segments are of increasingly shorter duration.

Figure 4 shows spectra at five different field strengths simulated with parameter sets A or B. All of the simulations
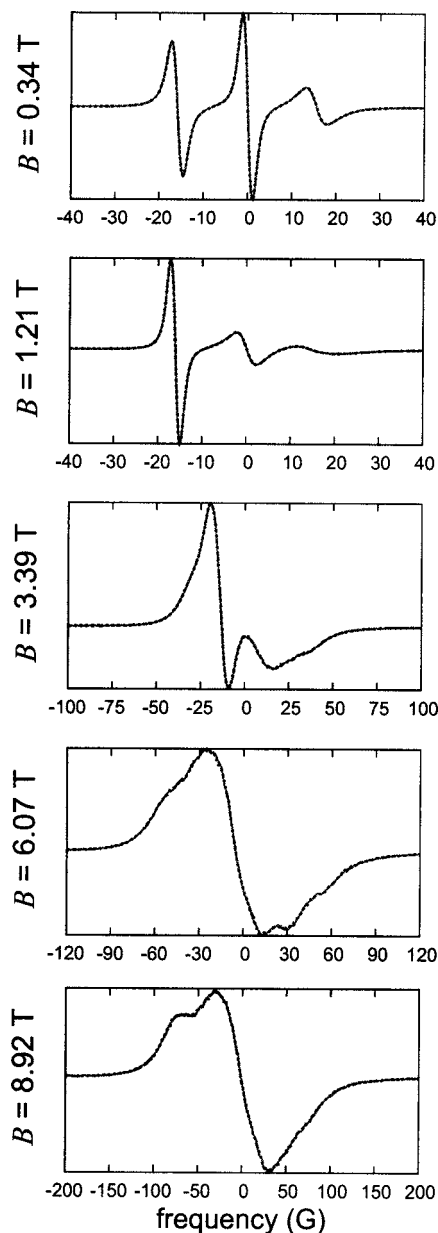
FIG. 4. Spectra at five different field strengths simulated from the MD trajectories with additional global tumbling ($D=18 \times 10^6$ s^{-1}) using integration parameters A (continuous) and B (dashed) in Table V. The magnetic tensors are given in Eq. (22).

FIG. 5. Spectra at $B_0=0.34$ T for rotational tumbling rates of $D=0$ and 6 $\times 10^6$ s^{-1}, simulated by using parameters B. The magnetic tensors are given in Eq. (22).

the X-band ESR spectra are concerned, the tumbling of the protein in 30 wt % sucrose solution can be completely disregarded, justifying the use of the MOMD model to fit such spectra.[51,53] In Fig. 5, we compare spectra simulated by combining the MD trajectories with stochastic rotational diffusion corresponding to $D=0$ and 6×10^6 s^{-1}, respectively. The latter (bottom spectrum) accounts for the effect of the global tumbling, whereas the former (top spectrum) corresponds to randomly oriented stationary molecules (powder spectrum). Clearly, the two spectra are significantly different. Explicit treatment of the tumbling, thus, appears to be crucial for the quantitative comparison of simulated and experimental spectra of T4L, even in 30 wt % sucrose solution.

IV. CONCLUDING DISCUSSION

A methodological framework for combining MD and stochastic trajectories in the time-domain simulation of FID ESR spectra was presented. Stochastic trajectories were used to account for tumbling dynamics that are slow and poorly sampled in atomistic MD simulations. Three methodological prerequisites were examined in detail. First, an accurate and efficient numerical scheme for propagating the quantum dynamics of the spins was proposed. This was achieved by working with the reduced density matrix in Hilbert space. Second, an accurate and efficient numerical scheme for the treatment of rotational Brownian diffusion was developed. Using quaternions instead of Euler angles to parametrize the relative orientation of two coordinate systems allowed us to easily treat the general case of restricted anisotropic diffusion. The familiar restricting potential, written as a sum of a few spherical harmonics, fits naturally into this formalism.

Time-domain spectral simulations performed with the developed quantal and classical integrators were compared to the well established spectral simulation methodology of Freed and co-workers based on the SLE. Excellent agreement was observed. Finally, time averaging of the magnetic tensors was introduced to bridge the gap between the fast time scale of the MD trajectories and the slow time scale of the quantum propagation. Averaging time windows appropriate for the simulations of spectra at different magnetic field strengths were estimated. The methodology of combining MD with stochastic trajectories was illustrated by using MD trajectories of a spin labeled, polyalanine α helix.

include the effect of isotropic tumbling with a diffusion coefficient $D=18 \times 10^6$ s^{-1}, in addition to the dynamics coming from the MD trajectories. The diffusion coefficient was chosen as representative of the global rotational diffusion of T4 lysozyme (T4L) in water at 22 °C.[31,32] The agreement between the spectra simulated with the two sets of parameters indicates that in this particular case, it is safe to use time steps Δt twice as large as the estimates in Table IV.

X-band (0.34 T) spectra of spin labeled T4L are often recorded in 30 wt % sucrose solution to reduce the narrowing effect of the global protein tumbling on the spectral lines.[49–52] Since this solution is about 3.3 times more viscous than an aqueous solution with no sucrose, the rotational diffusion coefficient of T4L is brought down to about $D=6 \times 10^6$ s^{-1}. Occasionally, it has been assumed that, as far as
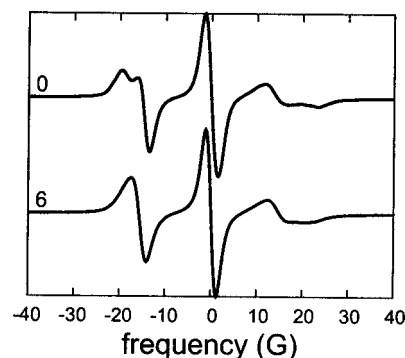
We would like to emphasize that the 18 MD trajectories considered in Sec. III C serve the sole purpose of illustrating the procedure, proposed in Sec. III, of combining atomistic trajectories, coming from BD or MD simulations, with stochastic trajectories. Although in a careful study of the simulated system, it would be important to assess whether the MD trajectories provide a complete coverage of the conformational space accessible to the spin label, this is not an issue addressed in this paper. The 18 MD simulations are intended to serve as a "typical" set of trajectories, expected from atomistic simulations of spin labeled proteins. These usually comprise just a few trajectories (on the order of 10), extending for a limited duration (tens of nanoseconds). Snapshots of the spin label are available with separation of about 1 ps, and the global tumbling of the system is too slow to be sampled in the simulations.

Previously, different ways of numerically integrating the spin dynamics of a nitroxide spin label have been proposed by Steinhoff and Hubbell,[20] by Eviatar *et al.*[26,34] and by Westlund and co-workers.[21,29] The approach of Steinhoff and co-workers, first introduced in Ref. [20] and more recently employed again in the context of using MD trajectories for spectral simulations,[23] considers only the eigenvalues of the instantaneous reduced Hamiltonian, disregarding the change of the eigenvectors with time. The equations in Refs. [20] and [23] are written for a single, complex scalar magnetization; thus, concern about a state vector or a density matrix becomes unnecessary and is not considered. Interpolation between the eigenvalues in the high-field and the pseudosecular approximations (in which not only the nonsecular but also the pseudosecular terms of the Hamiltonian are neglected) is introduced in an *ad hoc* fashion.[23] Since the three eigenvalues of the Hamiltonian are directly read from its entries, the quantum propagation reduces to updating the time-dependent phase of the magnetization.

Eviatar *et al.* developed a rigorous method to simulate ESR spectra of nitroxides in the time domain.[26] They propagate two state vectors in the reduced Hilbert space, as we discussed at the end of Sec. II A 2. The authors were reluctant to work with the density matrix because, as they state, "each trajectory describes the motion of a single molecule, and it is therefore impossible to implement any formalism, such as the density matrix, which implies that a calculation is carried out on an ensemble of spins."[34] In fact, one can think of the density matrix as a purely mathematical construct which emerges as a result of averaging over the initial conditions of the state vector. Eviatar *et al.* perform this averaging after the classical ensemble average over the trajectories. Because the quantum propagation along each random trajectory is linear and since the classical and quantum initial conditions are decoupled, exchanging the order of the two averages does not affect the final outcome.

In contrast, Usova *et al.* use the density operator, which they propagate in Liouville space.[29] They do not mention the high-field approximation but in their numerical integration scheme, only the $m_S = -\frac{1}{2}$, $m'_S = +\frac{1}{2}$ subspace of the full Liouville space is considered, which effectively imposes decoupled dynamics for the σ^{-+} sub-block of the density matrix. This is equivalent to neglecting the nonsecular terms and,

thus, invoking the high-field approximation. The authors propagate the (reduced) density matrix in Liouville space. The disadvantage of working in Liouville space, as opposed to using our Eq. (34), is not only due to the larger matrix representation of the (reduced) Liouvillian (9×9) compared to the Hamiltonian (3×3). Whereas in our formulation, the Hamiltonian can be easily and exactly exponentiated by using Eq. (37), this is not the case for the Liouvillian. Instead, the nondiagonal part of the Liouvillian has to be written as a sum of three matrices, each one of which can be exponentiated by using an equation similar to Eq. (37).[29] Since the exponential of the sum is not equal to the product of the separate exponentials, an approximation based on Trotter's formula has to be used.[29] As a result, evaluation of the short-time propagator in Liouville space contains five 9×9-matrix products. In comparison, using Eq. (34) with two 3×3-matrix products is not only exact but also more efficient.

Our treatment of rotational Brownian diffusion may be viewed as an extension of the work of Fedchenia *et al.* addressing isotropic rotational diffusion in a cone.[28] A stochastic differential equation for the quaternion was derived from what corresponds to our Eq. (43).[28] While this is appropriate for isotropic diffusion, handling anisotropic diffusion necessitates working with Eq. (46). In addition, whereas the conical potential shows its presence only at the (reflecting) boundary, the potentials studied in this paper continuously act during the diffusion. This enables the exact treatment of anisotropic diffusion in a potential. The only approximation is related to the finiteness of the integration time step. This is in contrast to Refs. [15] and [16], where jumps of constant arc length on the surface of a unit sphere are performed in the former, while the second Euler angle is discretized to start with in the latter. Both are limited to free isotropic diffusion.

Steinhoff and Hubbell developed a formalism,[20] which does include anisotropic rotational diffusion in a potential. In their presentation, no distinction is made between vector/tensor components referred to the body-fixed frame or the stationary frame. As we saw, this is the crucial difference between Eqs. (43) and (46). From the fact that an equation equivalent to Eq. (49) is used in Ref. [20], it can be assumed that all their equations are written in the body-fixed frame. The perfect agreement that our spectra show with spectra simulated by using the SLE (see Fig. 1) can be compared with a similar test for isotropic diffusion in Fig. 6 of Ref. [20]. It is hard to assess whether the reported discrepancy between the spectra in their work is due to the simplified propagation of the quantum dynamics or due to the treatment of the rotational diffusion.

Even when MD and stochastic trajectories are used together, as proposed in this paper, the demands on the number and duration of the MD trajectories are largely unrealistic for routine MD simulations of solvated spin labeled proteins. Currently, we are exploring ways of building stochastic, discrete-state Markov chain models from the MD trajectories and simulating the ESR spectra for the models, rather than directly using the MD trajectories. If successful, such an approach will replace the stochastic/MD dynamical model [Eq. (65)] with a purely stochastic one,

rotational   Markov

diffusion   chain

$$L \rightarrow M \rightarrow N. \tag{78}$$

The time-domain integrators developed in Sec. II and the time-averaging arguments of Sec. III remain equally useful for this model.

ACKNOWLEDGMENTS

APPENDIX A: MATRIX REPRESENTATIONS FOR EQUATION (37)

Defining $c_\theta = (\cos\theta - 1)$ and $s_\theta = -\sin\theta$, the real and imaginary parts of Eq. (37) are

$$\mathrm{Re}(e^{-i\theta\hat{N}}) = I_3 + \begin{pmatrix} c_\theta\left[n_z^2 + \left(\frac{1}{2}\right)(n_x^2 + n_y^2)\right] & \left(\frac{1}{\sqrt{2}}\right)[s_\theta n_y + c_\theta n_z n_x] & c_\theta\left(\frac{1}{2}\right)(n_x^2 - n_y^2) \\ \left(\frac{1}{\sqrt{2}}\right)[-s_\theta n_y + c_\theta n_z n_x] & c_\theta(n_x^2 + n_y^2) & \left(\frac{1}{\sqrt{2}}\right)[s_\theta n_y - c_\theta n_z n_x] \\ c_\theta\left(\frac{1}{2}\right)(n_x^2 - n_y^2) & \left(\frac{1}{\sqrt{2}}\right)[-s_\theta n_y - c_\theta n_z n_x] & c_\theta\left[n_z^2 + \left(\frac{1}{2}\right)(n_x^2 + n_y^2)\right] \end{pmatrix} \tag{A1}$$

and

$$\mathrm{Im}(e^{-i\theta\hat{N}}) = \begin{pmatrix} s_\theta n_z & \left(\frac{1}{\sqrt{2}}\right)[s_\theta n_x - c_\theta n_z n_y] & -c_\theta n_x n_y \\ \left(\frac{1}{\sqrt{2}}\right)[s_\theta n_x + c_\theta n_z n_y] & 0 & \left(\frac{1}{\sqrt{2}}\right)[s_\theta n_x + c_\theta n_z n_y] \\ c_\theta n_x n_y & \left(\frac{1}{\sqrt{2}}\right)[s_\theta n_x - c_\theta n_z n_y] & -s_\theta n_z \end{pmatrix}, \tag{A2}$$

where I_3 indicates the 3×3 identity matrix.

APPENDIX B: EULER ANGLES, QUATERNIONS, THE ROTATION MATRIX, AND ELEMENTS OF THE WIGNER ROTATION MATRICES

If the orientation of B with respect to S is given in terms of the Euler angles $\Omega = \{\alpha, \beta, \gamma\}$, the components of the corresponding quaternion can be calculated as[54]

$$q_0 = \cos(\beta/2)\cos((\gamma + \alpha)/2),$$

$$q_1 = \sin(\beta/2)\sin((\gamma - \alpha)/2),$$

$$q_2 = \sin(\beta/2)\cos((\gamma - \alpha)/2), \tag{B1}$$

$$q_3 = \cos(\beta/2)\sin((\gamma + \alpha)/2).$$

From the components of the quaternion, the 3×3 rotation matrix is calculated as[37]

$$R = \begin{pmatrix} q_0^2 + q_1^2 - q_2^2 - q_3^2 & 2q_1 q_2 - 2q_0 q_3 & 2q_1 q_3 + 2q_0 q_2 \\ 2q_1 q_2 + 2q_0 q_3 & q_0^2 - q_1^2 + q_2^2 - q_3^2 & 2q_2 q_3 - 2q_0 q_1 \\ 2q_1 q_3 - 2q_0 q_2 & 2q_2 q_3 + 2q_0 q_1 & q_0^2 - q_1^2 - q_2^2 + q_3^2 \end{pmatrix}. \tag{B2}$$

The matrix elements of R correspond to the direction cosines between the unit vectors $\underline{i}$ of the stationary coordinate system and the unit vectors $\underline{j}'$ of the rotating body-fixed frame,

$$R_{ij} = \underline{i} \cdot \underline{j}'. \tag{B3}$$

Therefore, the last row of R gives the components of $\underline{z}$ with respect to the axes of B, i.e., $R_{zx} = (\underline{z})_{x'}$, $R_{zy} = (\underline{z})_{y'}$, and $R_{zz} = (\underline{z})_{z'}$. For later convenience, we find it useful to introduce the notation

$$X \equiv R_{zx}, \quad Y \equiv R_{zy}, \quad Z \equiv R_{zz} \tag{B4}$$

for these matrix elements.

From the relation

$$\mathcal{D}^{1/2} = \begin{pmatrix} A & B \\ -B^* & A^* \end{pmatrix} = \begin{pmatrix} q_0 - iq_3 & -q_2 - iq_1 \\ q_2 - iq_1 & q_0 + iq_3 \end{pmatrix}, \tag{B5}$$

the matrix elements of $\mathcal{D}^1_{nm}$ and $\mathcal{D}^2_{nm}$ may be obtained (see Ref. 54). These are presented in Table VI, where $Z = R_{zz} = AA^* - BB^*$. The normalization condition (42) implies that $AA^* + BB^* = 1$.

Observe that

TABLE VI. Matrix elements of $\mathcal{D}^1_{nm}$ and $\mathcal{D}^2_{nm}$ from Ref. 54. The elements with $m < 0$ which are not shown may be obtained by using $\mathcal{D}^2_{n-m} = (-1)^{(n-m)}(\mathcal{D}^2_{-nm})^* \cdot (Z = AA^* - BB^*)$.

$\mathcal{D}^1_{nm}$	$+1$	0	-1
$+1$	A^2	$\sqrt{2}AB$	B^2
0	$-\sqrt{2}AB^*$	Z	$\sqrt{2}A^*B$
-1	B^{*2}	$-\sqrt{2}A^*B^*$	A^{*2}

$\mathcal{D}^2_{nm}$	$+2$	$+1$	0
$+2$	A^4	$2A^3B$	$\sqrt{6}A^2B^2$
$+1$	$-2A^3B^*$	$A^2(2Z-1)$	$\sqrt{6}ABZ$
0	$\sqrt{6}A^2B^{*2}$	$-\sqrt{6}AB^*Z$	$\frac{1}{2}(3Z^2-1)$
-1	$-2AB^{*3}$	$B^{*2}(2Z+1)$	$-\sqrt{6}A^*B^*Z$
-2	B^{*4}	$-2A^*B^{*3}$	$\sqrt{6}A^{*2}B^{*2}$

$$\mathcal{D}_{01}^1 = -\sqrt{2}(q_0 - iq_3)(-q_2 + iq_1) = -\frac{1}{\sqrt{2}}(X + iY),$$

$$\mathcal{D}_{0-1}^1 = -\mathcal{D}_{01}^{1*} = \frac{1}{\sqrt{2}}(X - iY), \tag{B6}$$

as can be determined from Table VI. Furthermore,

$$\mathcal{D}_{0\pm1}^2 = \sqrt{3}\mathcal{D}_{0\pm1}^1 Z = \mp\sqrt{\frac{3}{2}}(X \pm iY)Z,$$

$$\mathcal{D}_{0\pm2}^2 = \frac{\sqrt{6}}{2}(\mathcal{D}_{0\pm1}^1)^2 = \frac{\sqrt{6}}{4}(X \pm iY)^2. \tag{B7}$$

These results will be used below.

APPENDIX C: EXPRESSIONS FOR SOME POTENTIAL ENERGY FUNCTIONS

A few special cases of $u(\Omega)$ are treated in detail. First, let us look at

$$u(\Omega) = -c_0^1 \mathcal{D}_{00}^1(\Omega) = -c_0^1 Z. \tag{C1}$$

For positive c_0^1, this potential tries to keep the axes $\underline{z}$ and $\underline{z}'$ aligned, penalizing orientations in which $Z = \underline{z} \cdot \underline{z}'$ moves away from $Z = 1$. The expressions (59) in this case reduce to

$$-iJ_x u = \frac{-i}{\sqrt{2}}c_0^1[\mathcal{D}_{01}^1 + \mathcal{D}_{0-1}^1] = -c_0^1 Y,$$

$$-iJ_y u = \frac{-1}{\sqrt{2}}c_0^1[\mathcal{D}_{01}^1 - \mathcal{D}_{0-1}^1] = c_0^1 X, \tag{C2}$$

$$-iJ_z u = 0.$$

where the last equalities follow from Eq. (B5). Now, we consider the potential

$$u(\Omega) = -c_{-1}^1[\mathcal{D}_{0-1}^1(\Omega) - \mathcal{D}_{01}^1(\Omega)] = -\sqrt{2}c_{-1}^1 X, \tag{C3}$$

i.e., $c_1^1 = -c_{-1}^1$. Again, for positive c_{-1}^1, this potential tries to keep the $\underline{z}$ and $\underline{x}'$ axes aligned. Substitution of $u(\Omega)$ in Eq. (59) yields

$$-iJ_x u = \frac{-i}{\sqrt{2}}c_{-1}^1[\mathcal{D}_{00}^1 - \mathcal{D}_{00}^1] = 0,$$

$$-iJ_y u = -\sqrt{2}c_{-1}^1\mathcal{D}_{00}^1 = -\sqrt{2}c_{-1}^1 Z, \tag{C4}$$

$$-iJ_z u = ic_{-1}^1[\mathcal{D}_{0-1}^1 + \mathcal{D}_{01}^1] = \sqrt{2}c_{-1}^1 Y.$$

Putting everything together, for the potential

$$u(\Omega) = -c_0^1 \mathcal{D}_{00}^1(\Omega) - c_{-1}^1[\mathcal{D}_{0-1}^1(\Omega) - \mathcal{D}_{01}^1(\Omega)], \tag{C5}$$

we obtain

$$-iJ_x u = -c_0^1 Y$$

$$-iJ_y u = c_0^1 X - \sqrt{2}c_{-1}^1 Z \tag{C6}$$

$$-iJ_z u = \sqrt{2}c_{-1}^1 Y.$$

The potential

$$u(\Omega) = -c_0^2 \mathcal{D}_{00}^2(\Omega) = -c_0^2 \frac{1}{2}(3Z^2 - 1) \tag{C7}$$

favors orientations in which $\underline{z}$ and $\underline{z}'$ are either parallel or antiparallel ($Z = \pm1$). As before, by using Eq. (B6), one finds

$$-iJ_x u = -i\sqrt{\frac{3}{2}}c_0^2[\mathcal{D}_{01}^2 + \mathcal{D}_{0-1}^2] = -3c_0^2 YZ,$$

$$-iJ_y u = -\sqrt{\frac{3}{2}}c_0^2[\mathcal{D}_{01}^2 - \mathcal{D}_{0-1}^2] = 3c_0^2 XZ, \tag{C8}$$

$$-iJ_z u = 0.$$

Finally, we treat the potential

$$u(\Omega) = -c_2^2[\mathcal{D}_{02}^2(\Omega) + \mathcal{D}_{0-2}^2(\Omega)] = -c_2^2\frac{\sqrt{6}}{2}(X^2 - Y^2), \tag{C9}$$

i.e., $c_2^2 = c_{-2}^2$. This potential prefers orientations in which $\underline{z}$ is parallel or antiparallel to $\underline{x}'$ ($X = \pm1$) and disfavors orientations in which $\underline{z}$ is parallel or antiparallel to $\underline{y}'$ ($Y = \pm1$). We find from Eq. (59) that

$$-iJ_x u = -ic_2^2[\mathcal{D}_{0-1}^2 + \mathcal{D}_{01}^2] = -\sqrt{6}c_2^2 YZ,$$

$$-iJ_y u = -c_2^2[\mathcal{D}_{0-1}^2 - \mathcal{D}_{01}^2] = -\sqrt{6}c_2^2 XZ, \tag{C10}$$

$$-iJ_z u = -2ic_2^2[\mathcal{D}_{02}^2 - \mathcal{D}_{0-2}^2] = 2\sqrt{6}c_2^2 XY.$$

Clearly, for the general potential,

$$u(\Omega) = -c_0^2 \mathcal{D}_{00}^2 - c_2^2[\mathcal{D}_{02}^2(\Omega) + \mathcal{D}_{0-2}^2(\Omega)], \tag{C11}$$

we simply need to sum the above expressions to obtain

$$-iJ_x u = (-3c_0^2 - \sqrt{6}c_2^2)YZ,$$

$$-iJ_y u = (3c_0^2 - \sqrt{6}c_2^2)XZ, \tag{C12}$$

$$-iJ_z u = 2\sqrt{6}c_2^2 XY.$$

[1] W. L. Hubbell, D. S. Cafiso, and C. Altenbach, Nat. Struct. Biol. **7**, 735 (2000).
[2] P. P. Borbat, A. J. Costa-Filho, K. A. Earle, J. K. Moscicki, and J. H. Freed, Science **291**, 266 (2001).
[3] B. H. Robinson, C. Mailer, and G. Drobny, Annu. Rev. Biophys. Biomol. Struct. **26**, 629 (1997).
[4] R. Kubo, J. Phys. Soc. Jpn. **26**, 1 (1969).
[5] R. Kubo, Adv. Chem. Phys. **15**, 101 (1969).
[6] R. Kubo, J. Phys. Soc. Jpn. **9**, 935 (1954).
[7] J. H. Freed, G. V. Bruno, and C. F. Polnaszek, J. Phys. Chem. **75**, 3385 (1971).
[8] C. F. Polnaszek, G. V. Bruno, and J. H. Freed, J. Chem. Phys. **58**, 3185 (1973).
[9] E. Meirovitch, A. Nayeem, and J. H. Freed, J. Phys. Chem. **88**, 3454 (1984).
[10] A. Polimeno and J. H. Freed, Adv. Chem. Phys. **83**, 89 (1993).
[11] A. Polimeno and J. H. Freed, J. Phys. Chem. **99**, 10995 (1995).
[12] D. E. Budil, S. Lee, S. Saxena, and J. H. Freed, J. Magn. Reson., Ser. A **120**, 155 (1996).
[13] Z. Liang and J. H. Freed, J. Phys. Chem. B **103**, 6384 (1999).
[14] M. Saunders and C. S. Johnson, Jr., J. Chem. Phys. **48**, 534 (1968).
[15] J. B. Pedersen, J. Chem. Phys. **57**, 2680 (1972).
[16] B. H. Robinson, L. J. Slutsky, and F. P. Auteri, J. Chem. Phys. **96**, 2609 (1992).
[17] P. Hakansson, L. Persson, and P.-O. Westlund, J. Chem. Phys. **117**, 8634 (2002).

[18] L. Persson, U. Cegrell, N. Usova, and P.-O. Westlund, J. Math. Chem. **31**, 65 (2002).

[19] H. Eviatar, U. van der Heide, and Y. K. Levine, J. Chem. Phys. **102**, 3135 (1995).

[20] H.-J. Steinhoff and W. Hubbell, Biophys. J. **71**, 2201 (1996).

[21] P. Hakansson, P.-O. Westlund, E. Lindahl, and O. Edholm, Phys. Chem. Chem. Phys. **3**, 5311 (2001).

[22] I. Stoica, J. Phys. Chem. B **108**, 1771 (2004).

[23] C. Beier and H.-J. Steinhoff, Biophys. J. **91**, 2647 (2006).

[24] J. H. Freed, Annu. Rev. Phys. Chem. **51**, 655 (2000).

[25] D. Sezer, J. H. Freed, and B. Roux, "Parametrization, Molecular Dynamics Simulation, and Calculation of Electron Spin Resonance Spectra of a Nitroxide Spin Label on a Polyalanine α-Helix," J. Phys. Chem. B (in press); available online at http://pubs.acs.org/cgi-bin/abstract.cgi/jpcbfk/asap/abs/jp711375x.html.

[26] H. Eviatar, E. van Faassen, Y. Levine, and D. Hoult, Chem. Phys. **181**, 369 (1994).

[27] D. E. Budil, K. L. Sale, K. A. Khairy, and P. G. Fajer, J. Phys. Chem. A **110**, 3703 (2006).

[28] I. I. Fedchenia, P.-O. Westlund, and U. Cegrell, Mol. Simul. **11**, 373 (1993).

[29] N. Usova, P.-O. Westlund, and I. Fedchenia, J. Chem. Phys. **103**, 96 (1995).

[30] A. Abragam, *Principles of Nuclear Magnetism* (Oxford University Press, Oxford, 1961).

[31] Z. Liang, Y. Lou, J. H. Freed, L. Columbus, and W. L. Hubbell, J. Phys. Chem. B **108**, 17649 (2004).

[32] J. P. Barnes, Z. Liang, H. S. Mchaourab, J. H. Freed, and W. L. Hubbell, Biophys. J. **76**, 23298 (1999).

[33] S. L. Altmann, *Rotations, Quaternions and Double Groups* (Dover, New York, 2005).

[34] H. Eviatar, Y. K. Levine, and D. I. Hoult, J. Magn. Reson., Ser. A **117**, 41 (1995).

[35] Y. P. Kalmykov, Phys. Rev. E **65**, 021101 (2001).

[36] W. T. Coffey, Y. P. Kalmykov, and J. T. Waldron, *The Langevin Equation with Applications to Stochastic Problems in Physics, Chemistry, and Electrical Engineering*, 2nd ed. (World Scientific, Singapore, 2004).

[37] L. C. Biedenharn and J. D. Louck, *Angular Momentum in Quantum Physics: Theory and Application* (Addison-Wesley, Reading, MA, 1981).

[38] A. Ponti, J. Magn. Reson. **138**, 288 (1999).

[39] R. R. Ernst, G. Bodenhausen, and A. Wokaun, *Principles of Nuclear Magnetic Resonance in One and Two Dimensions* (Oxford University Press, Oxford, 1987).

[40] The referee has called our attention to the work of S. D. DeSensi, D. P. Rangel, A. H. Beth, T. P. Lybrand, and E. J. Hustedt, Biophys. J. (in press); available online at http://www.biophysj.org/.

[41] N. G. Van Kampen, Phys. Rep. **124**, 69 (1985).

[42] C. P. Slichter, *Principles of Magnetic Resonance*, 3rd ed. (Springer Verlag, 1990).

[43] B. R. Brooks, R. E. Bruccoleri, B. D. Olafson, D. J. States, S. Swaminathan, and M. Karplus, J. Comput. Chem. **4**, 187 (1983).

[44] T. Darden, D. York, and L. Pedersen, J. Chem. Phys. **98**, 10089 (1993).

[45] U. Essmann, L. Perera, M. L. Berkowitz, T. Darden, H. Lee, and L. G. Pedersen, J. Chem. Phys. **103**, 8577 (1995).

[46] G. Lamoureux and B. Roux, J. Chem. Phys. **119**, 3025 (2003).

[47] S. E. Feller, R. W. Pastor, A. Rojnuckarin, S. Bogusz, and B. R. Brooks, J. Phys. Chem. **100**, 17011 (1996).

[48] I.-C. Yeh and G. Hummer, Biophys. J. **86**, 681 (2004).

[49] H. S. Mchaourab, M. A. Lietzow, K. Hideg, and W. L. Hubbell, Biochemistry **35**, 7692 (1996).

[50] H. S. Mchaourab, T. Kalai, K. Hideg, and W. L. Hubbell, Biochemistry **38**, 2947 (1999).

[51] L. Columbus, T. Kalai, J. Jeko, K. Hideg, and W. L. Hubbell, Biochemistry **40**, 3828 (2001).

[52] Z. Guo, D. Cascio, K. Hideg, T. Kalai, and W. L. Hubbell, Protein Sci. **16**, 1069 (2007).

[53] L. Columbus and W. L. Hubbell, TIBS **27**, 288 (2002).

[54] R. M. Lynden-Bell and A. J. Stone, Mol. Simul. **3**, 271 (1989).